Enhancing the Matrix Addressing of Flexible Sensory Arrays by a Highly Nonlinear Threshold Switch

Ming Wang[1], Wei Wang[2], Wan Ru Leow[1], Changjin Wan[1], Geng Chen[1], Yi Zeng[1], Jiancan Yu[1], Yaqing Liu[1], Pingqiang Cai[1], Hong Wang[1], Daniele Ielmini[2†] and Xiaodong Chen[1†]

[1]Innovative Centre for Flexible Devices (iFLEX), School of Materials Science and Engineering, Nanyang Technological University, 50 Nanyang Avenue, Singapore 639798, Singapore.

[2]Dipartimento di Elettronica, Informazione e Bioingegneria, Politecnico di Milano, Piazza L. da Vinci 32 – 20133, Milano, Italy.

[†]Corresponding author. E-mail: daniele.ielmini@polimi.it; chenxd@ntu.edu.sg

The increasing need for smart systems in healthcare, wearable, and soft robotics is creating demand for low-power sensory circuits that can detect pressure, temperature, strain, and other local variables. Among the most critical requirements, the matrix circuitry to address the individual sensor device must be sensitive, immune to disturbances, and flexible within a high-density sensory array. Here, a strategy is reported to enhance the matrix addressing of a fully integrated flexible sensory array with an improvement of 10^8 fold in the maximum readout value of impedance by a bidirectional threshold switch. The threshold switch shows high flexibility (bendable to a radius of about 1 mm) and a high nonlinearity of $\approx 10^{10}$ by using a nanocontact structure strategy, which is revealed and validated by molecular dynamics simulations and experiments at variable mechanical stress. Such a flexible electronic switch enables a new generation of large-scale flexible and stretchable electronic and optoelectronic systems.

Flexible electronic circuits for pressure, temperature, strain, electrochemical, and gas sensing have been recently proposed with promising applications in healthcare[1-4], wearable electronics[4-6] and robotics[2, 7, 8]. For these applications, the crossbar array of sensory devices is an enabling technology offering low cost, high density, low power, large area and mechanical flexibility[7]. However, the practical integration of these crossbar arrays is hindered by the notorious issue of crosstalk, which arises due to the sneak path currents from neighboring elements deteriorating the operational attributes of the array[7, 9]. To enable correct read out of the array, an electronic switch possessing a nonlinear response, most typically a field-effect transistor (FET), is usually connected to a functional element to suppress the sneak path currents[7, 8, 10-13]. Recently, selection elements based on field-induced threshold switching (TS) phenomena have received considerable attention due to its two-terminal structure, low operation voltage and 3D stacking capability in crossbar arrays for high density memory circuits[14-16]. These properties make the TS device extremely attractive for flexible electronic and optoelectronic integration, such as electronic displays, sensory circuits, information storage, and data processing.

To alleviate the sneak path issue in crossbar arrays, selection elements with high ON-state current and high nonlinearity, i.e., the ratio between the current at the read voltage (V_D) and at half read voltage ($\frac{1}{2}V_D$), are needed [14, 17-19]. These properties can be provided by the TS phenomena, where a conductive filament is formed in correspondence to a characteristic electric field, and dissolved spontaneously as the external electrical field is reduced below the threshold[14, 20]. This process is controlled by two critical parameters, namely the diffusivity of migrating species and external driving forces, e.g., the surface energy (Gibbs–Thomson effect)[15, 20-22] and mechanical stress[20, 23] of the conductive filament. The diffusivity of migrating species can be improved by engineering the materials, e.g., by doping the dielectric layer with fast diffusive particles[15, 16]. However, the reported TS devices are rigid and not suitable for sensor applications in healthcare, wearable electronics and soft robotics, where high mechanical flexibility is required. Alternatively, low compliance current (CC) is another method[24, 25] commonly used to induce the TS phenomena because it leads to the formation of thin conductive filaments with high surface energy that rupture easily and induce the OFF-state, as observed by *in situ* high-resolution transmission electron microscopy (HRTEM)[14, 15, 24, 26]. However, at low CC, the ON-state current level and nonlinearity may deteriorate significantly. On the other hand, the reliability of TS devices is compromised at high CC. Therefore, there is a trade-off between achieving high nonlinearity and high reliability in TS devices.

To address the current challenges of TS devices, we developed a flexible TS device for selecting sensor elements in a flexible pressure sensor array. Our TS device is based on a nanocomposite thin film consisting of an elastic insulating matrix and an electrically conducting filler of silver nanowires (AgNWs), which confers flexibility and forms a nanoscale conductive filament via the nano-contact effect. The two-terminal bidirectional flexible TS device shows an unprecedented nonlinearity of 10^{10} and good mechanical flexibility with bending radius r approaching 1 mm. To quantitatively explain the TS behavior, we proposed a switching model based on minimization of interfacial energy and thermal diffusion, and validated the model

experimentally at variable mechanical stress. An integrated flexible TS-based sensory array with significantly improved readout range for individual pressure sensor elements was experimentally demonstrated.

Nano-contact improves TS behavior

To understand the underlying mechanism of nano-contact active electrodes, we fabricated and characterized three TS devices with different contact morphologies (Fig. 1a). Device I had a thin film silver electrode, device II and III, which contain AgNW structures in the electrodes, took on a single-sided nanowire (SSNW) and a double-sided nanowire (DSNW) electrode configuration, respectively (see Supplementary Figure 1 and Supplementary Text 1 for device configurations and fabrication process flows). To validate the universality of the nano-contact strategy, we used both silk fibroin and polydimethylsiloxane (PDMS) elastomer as the device dielectrics. Based on the evolution of current-voltage (*I-V*) characteristics as a function of the CC, the maximum allowed CC for reliable TS operation for devices I, II, and III are 10^{-7} A, 10^{-4} A, and 10^{-3} A, respectively (Supplementary Fig. 2). We conducted the statistical probability of TS, defined by a retention time of the ON-state resistance being less than 5 s, as a function of the CC for the three device configurations (Fig. 1b). Compared to device I with thin film electrodes, device II and III with AgNW electrodes showed a more reliable TS behavior under high CC, and this is attributed to the nano-contact effect of the AgNW electrodes. The TS probability of ~ 100% in device III could be achieved for a broad range of CC reaching up to about 1 mA. Even for a CC of about 3 mA, the TS behavior could still be observed in device III (Supplementary Fig. 3a), which is the highest CC of volatile switching reported so far[14, 16]. A high CC allowed for the reliable TS behavior guarantees high nonlinearity and ON-state current of the selection operation. Note that only device III shows the bidirectional switch behavior (Supplementary Fig. 3b), which can be attributed to its symmetrical physical structure. These results demonstrate that the nano-contact approach can be used to improve the TS behavior, allowing highly reliable and nonlinear TS devices to be designed. The DSNW-type sample can be easily achieved by natural nano-contacts between AgNW

fillers in the nanocomposite thin film, where the nano-gap can be properly mediated by the concentration of the filler.

Electrical and mechanical properties of the flexible TS device

We used the nano-contact strategy to obtain highly nonlinear flexible TS devices. The flexible TS device consists of two planar Au electrodes sandwiching an elastic composite thin film, made up of AgNWs dispersed in PDMS elastomer (Fig. 1c; see Supplementary Fig. 4 and Methods for detailed fabrication process). Scanning electron microscopy (SEM) images show a randomly oriented network of AgNWs embedded in the surface layer of the PDMS elastomer (Supplementary Fig. 5a). Only a fraction of AgNWs is exposed at the very top of the PDMS elastomer, while the majority of them are firmly buried in the bulk of the elastomer, thus guaranteeing good mechanical stability of the nanostructure[27] (Inset of Fig. 1e).

The as-prepared Au/AgNWs-PDMS/Au flexible TS device with high initial OFF resistance state (10^{13} Ω) requires an electroforming process with the application of a forming voltage around 2.5 V to activate the bidirectional TS behavior[14] (Supplementary Fig. 5b). Fig. 1d shows the typical TS characteristics of the flexible TS device with a CC of 500 μA after the forming process. The current is initially very low in the OFF-state until it abruptly increases to the ON-state at a threshold voltage of about 0.4 V, also referred to as the turn-on voltage, V_{ON}. The flexible TS device then spontaneously returns to the OFF-state as the applied voltage sweeps back to zero, contrary to the resistive switching behavior in memory switching devices[24, 25, 28, 29]. Similar *I-V* characteristics of TS were observed under negative polarity, indicating a symmetric bidirectional switching behavior, which is highly desired for selection elements in combination with bipolar resistive switching devices[14, 17, 30]. The maximum value of nonlinearity, which is a key figure of merit to assess the performance of a selection element, is more than 10^{10} at V_D = 0.5 V (Fig. 1e), which is the highest reported in flexible TS devices with bidirectional switching and could compete with state-of-art silicon-based electronic switches (Supplementary Fig. 6). The huge

nonlinearity is also accompanied by an extremely steep slope of below 4 mV • dec^{-1}.

For practical application of the flexible TS, device uniformity, speed, and reliability are also important aspects. Fig. 2a shows 200 repeated *I-V* curves, which were consecutively obtained under *DC* operation in an individual flexible TS device. The data show no remarkable deterioration, indicating excellent reliability. The device-to-device uniformity was tested by collecting data from ten individual devices (Supplementary Fig. 7), with all devices showing repeatable and reliable bidirectional TS behavior. It should be mentioned that the turn-on voltages of the flexible TS device in this study can be intentionally tuned by controlling the concentration of AgNWs sprayed on the silicon wafer (Supplementary Fig. 8), which matches well with the various functional elements in the integration array. The measured dynamical current response characteristics of the flexible TS device corresponding to a voltage pulse are shown in Fig. 2b. The device shows fast switching (~ 520 ns; see inset of Fig. 2b) to the ON-state under an applied pulse, but requires a relaxation time to recover to its original OFF-state after the voltage is switched to zero[14, 15]. The characteristic relaxation time roughly ranges from 50 μs to 400 μs (Supplementary Fig. 9), in agreement with previous results[23]. The fast relaxation characteristics of the flexible TS device are sufficient for most flexible functional sensory elements, which typically show a relaxation time of 1 ms to 10 s[31, 32]. The flexible TS device can withstand an endurance of over 10^6 cycles under the 100 μs / 2 V programming pulses and 100 μs / 0.3 V read pulses, with a 1.8 ms wait time between each program and read pulse (Fig. 2c). In addition, the read disturb test showed no resistance degradation under various constant voltage stress of $V_D = \pm 0.6$ V and $1/2V_D = \pm 0.3$ V, which further demonstrates the excellent immunity to read disturbance (Supplementary Fig. 10).

Our flexible TS device also showed excellent mechanical stability under bending. The experimental setup for the mechanical bending test is illustrated in the Methods section and Supplementary Fig. 11a. Compared to the original state of the flexible TS device, the *I-V* characteristics show no obvious change under the curved state with a bending radius *r* of 4.9 mm (Fig. 2d). In particular, the super nonlinear TS behavior is

still observed even under extreme stress conditions of rolling on a needle of radius ~ 1 mm, the only effect being an increase of the turn-on voltage (Supplementary Fig. 11b), thus indicating a robust mechanical reliability. We further tested the TS behavior of the flexible TS device under both bending directions. Fig. 2e shows the distributions of both positive (+ V_{ON}) and negative (- V_{ON}) turn-on voltages under both inward bending ($r < 0$) and outward bending ($r > 0$), as a function of the reciprocal of the bending radius. The flexible TS device shows an excellent mechanical bending flexibility over a wide range ($-0.4\ mm^{-1} < r^{-1} < 0.2\ mm^{-1}$) with a slight change in the turn-on voltages. The turn-on voltages increase when the bending radius, r, is less than 4 mm, but the device could still maintain a typical TS behavior without any loss of ON/OFF ratio (Supplementary Fig. 11c). The increase of the turn-on voltages is attributed to the mechanical strain increasing the distance between two adjacent AgNWs in the PDMS elastomer (Supplementary Fig. 12a, b). Moreover, we tested the reversibility of flexible TS device under bending conditions ($r = 5$ mm) (Methods section), as shown in Fig. 2f. The *I-V* characteristics of the flexible TS device during consecutive 1000 mechanical bending cycles show no noticeable deterioration. These results indicate that the flexible TS device exhibits robust mechanical stability and reliability, even under harsh substrate physical deformation, such as the twisted state (Supplementary Fig. 11d).

Diffusive dynamics switching mechanism

Understanding the underlying switching mechanism is vital to improve the design and performance of the flexible TS device. To probe the role of AgNWs in highly-nonlinear TS behavior, we compared the behavior of the TS device with another device fabricated in exactly the same way but using a carbon nanotubes (CNTs)-PDMS nanocomposite thin film instead. The *I-V* curves of the Au/CNTs-PDMS/Au devices show no reversible resistive switching behavior regardless of the concentration of CNTs (Supplementary Fig. 13), which is consistent with the observed results in bulk nanocomposites[33]. Compared to inert CNTs, AgNWs show high surface chemical activity and electrochemical mobility[20, 33], which are critical for inducing the TS behavior. Furthermore, it is well known that silver (Ag) conductive filaments are easily formed

in conductive bridging random access memory (CBRAM) with an active Ag electrode. Therefore, field-induced formation of Ag conductive filaments bridging adjacent AgNW clusters could explain the TS from OFF-state to ON-state. In the flexible TS device, two adjacent AgNWs might serve as the effective top and bottom electrodes to extend the percolation network in the AgNWs-PDMS nanocomposite thin film, which further identifies the Au/AgNWs-PDMS/Au device as a DSNW-type structure (inset of Fig. 1c).

To gain a deeper insight into the TS behavior of flexible TS device, we performed a molecular dynamics simulation based on an overdamped Langevin model (Methods). In these simulations, ionic migration/diffusion is described under the influence of Joule heating, electric field, interfacial energy minimization and Gibbs–Thomson effect. The electrochemical redox reactions were neglected because their effect on the spontaneous return to the OFF-state upon removal of the external bias is negligible[14, 15]. The simulated and experimental *I-V* characteristics of the flexible TS device under both positive and negative voltages show excellent agreement in the bidirectional TS behavior, supporting the validity of the molecular dynamics Langevin model (Fig. 3a). The simulated dynamic evolution of the nanoscale Ag filament as a function of the sweep voltage is shown in Fig. 3b. In the initial stage of the simulation, two silver clusters (including 30 silver nanoparticles each) are separately located nearby the two adjacent AgNWs (OFF-state in Fig. 3c). When a positive sweep voltage is applied, the silver cluster located on the positive polarity begin to break up into nanoparticles due to localized Joule heating under electrical field, and move towards the opposite AgNW as a result of the applied electrical field and concentration gradient. Until a certain critical voltage, only a few silver nanoparticles can uniformly fill the gap between the adjacent AgNWs to form an electrically connected filament in a fast time scale (see Fig. 3b○,2). Due to the CC and nanoconfinement effect of AgNWs, the formed filament should be in an extremely tiny size scale, which retains a large interfacial energy due to the Gibbs–Thomson effect[21]. When the positive voltage decreases, the formed filament spontaneously breaks up and collapses into larger

clusters to minimize the interfacial energy nearby the two adjacent AgNWs. This process is similar to Rayleigh instability of nanowires with anisotropic surface energy[34]. Also, Nernst potential may further accelerate the dissolution of the filament. These effects eventually lead to TS behavior of the flexible TS device under both positive and negative sweep voltages. Schematic in Fig 3c illustrates the volatile TS process; the formation and rupture of Ag conductive filaments bridging adjacent AgNWs results in the OFF- and ON-state of the flexible TS device.

The model also considers the role of the bending radius in the diffusive dynamics (Methods). We simulated the TS behavior of the flexible TS device at the positive sweep voltage under various bending radii (Fig. 3d), which is similar to the measured *I-V* curves for both inward bending ($r < 0$) and outward bending ($r > 0$). Similar simulated *I-V* curves were found for negative sweep voltage (Supplementary Fig. 12d). From the simulation results, the positive turn-on voltage (+ V_{ON}) increases for increasing $1/r$, reaching about 3 V for $r \sim 1$ mm, in good agreement with the experimental results in Fig. 2e. These results further demonstrate the validity of the proposed diffusive dynamics model. Note that the mechanical stress effects at the conductive filament, which were not taken into account in this model, might still have a significant role in the relaxation of the ON-state[23, 35].

Improving the readout range of flexible TS-based sensory arrays

The two-terminal transistor-free structure of the flexible TS device allowed us to develop a flexible crossbar array that integrates large-scale sensor elements for practical applications (see Fig 4a). In this configuration, each cross-point consists of a two-terminal flexible TS device and a sensor device connected in series to form an integrated unit (left inset of Fig. 4a). To demonstrate this concept, we fabricated an ultrasensitive pressure sensor (see Methods), consisting of a pyramidal PDMS substrate (inset of Fig. 4b) coated by a single-walled carbon nanotubes (CNT) layer[31, 36], which exhibits reliable sensing characteristics as shown by the pressure-impedance relationship (Fig. 4b). To evaluate crosstalk effects, we firstly investigated the

performance of an integrated unit within the crossbar array. In an integrated unit, the individual CNT pressure sensor always shows nearly linear *I-V* characteristics regardless of load pressure (Fig. 4c), and the individual flexible TS device exhibits a typical TS behavior (Fig. 4d). After integration, the current at low voltage (< 0.6 V) was effectively suppressed by the flexible TS device, while current at high bias voltage was used to accurately sense the load pressure due to ON-state of the flexible TS device (Fig. 4e). By setting V_D to 0.8 V, we verified that the nonlinearity of the integrated unit is as high as 10^8 for a load pressure of 748 Pa, which may effectively alleviate the crosstalk issue in sensory arrays.

Further, a fully integrated 2 × 2 flexible TS-based pressure sensor array was fabricated (Fig. 5a, see Methods for fabrication process). Multi-level load pressures were continuously monitored in real time for an e-skin application using the 2 × 2 flexible pressure sensor array. For simplicity, the flexible pressure sensor array was attached onto a 3D printed hand replica and the probe station system was used to provide and measure the real load pressure (Fig. 5b). To evaluate the crosstalk issue, two flexible pressure sensor arrays with flexible TS-based array backplane (W/TS) and without flexible TS-based array backplane (WO/TS) were implemented to monitor the real-time and continuous load pressure. In the worst-case scenario where all unselected pixels (R_U) are subject to maximum load pressure, the selected word line (WL) is biased to V_D and the selected bit line (BL) is biased to 0 V, while all the unselected WLs and BLs are floating[19, 37]. We can clearly see in the upper panel of Fig 5c that due to the leakage current flowing through the other three pixels ($R_{U1} + R_{U2} + R_{U3}$) in the WO/TS array (inset in Fig 5c), the resistance value of the selected pixel (R_S) was pinched to a fixed value of 27 kΩ (corresponding to 1763 Pa pressure) . However, sneak current path in the W/TS array was eliminated and real load pressures could be accurately detected over a broad range (lower panel of Fig. 5c). Fig. 5d shows the enabled readout range of a selected pixel as a function of real load pressure in two types of array; the readout range is significantly improved by inducing the flexible TS-based array backplane.

To further evaluate the performance of large-scale integration array, we calculated

the read margin at worst-case scenario in a one bit-line pull-up (OBPU) scheme (Supplementary Text 2 and Supplementary Fig. 14)[37, 38]. The maximum array size (taking 10% read margin as the criterion) of the flexible TS-based array backplane as a function of the number of WLs = BLs is presented in Fig. 5e. If we assume that all unselected pixels are 10^4 Ω, the calculated maximum array size can reach up to 10^7, which is sufficient for most electronic and optoelectronic applications in large-scale integration.

Conclusion

In conclusion, we have constructed and demonstrated a new class of flexible and super nonlinear TS device using the nano-contact strategy. The fabricated flexible TS device shows a super nonlinearity of 10^{10}, high ON-state current of 500 μA, and robust mechanical flexibility. The TS behavior in the nanocomposite was further revealed by molecular dynamics simulation. Furthermore, we experimentally demonstrated that the flexible TS device is able to solve the crosstalk issue in a fully integrated flexible pressure array with a significantly improved readout range. These results provide a promising pathway toward large-scale integration of flexible electronic and optoelectronic devices by utilizing transistor-free TS switches.

Experimental section

Fabrication of the Flexible TS Device: Silver nanowires (60 nm × 10 μm, 0.5 wt% in isopropyl alcohol) and PDMS were purchased from Sigma-Aldrich. First, 1 mL of AgNW solution was diluted to an extremely low concentration (0.012 wt%) for inkjet printing by adding 40 mL of isopropyl alcohol solution. Then, a silicon wafer after hydrophobization treatment was patterned by a shadow mask and was placed onto a hotplate at 80 °C. Subsequently, the diluted AgNW solution was sprayed on the silicon substrate by the inkjet printing method to form a uniform conductive film (≈1 kΩ) of AgNW network. The shadow mask was removed and the liquid PDMS precursors were poured with a weight ratio of 8:1 (the silicone prepolymer:the crosslinker). Then, it was cured in an oven at 60 °C for 10 h. The AgNW–PDMS nanocomposite film was peeled off from the silicon substrate. Finally, 70 nm thickness Au planar electrodes were deposited on the region of nanocomposite film by thermal evaporator. The space of two planar Au electrodes was 50 μm.

Fabrication of the Flexible TS-Based Sensory Array: First, an ultrasensitive CNT pressure sensor array was fabricated by using a pyramidal silicon master after hydrophobization treatment. The pyramid pattern size of the silicon master was 35 μm × 35 μm. PDMS precursor was mixed in a ratio of 10:1 and was poured on the pyramidal silicon master. After curing at 60 °C for 10 h, it was peeled off to obtain the PDMS substrate with pyramid patterns. Furthermore, the pyramidal PDMS substrate was patterned into a 2 × 2 array (individual cell: 1.2 mm × 1.5 mm) by the adhesive tape. About 1 g L−1 of single-walled carbon nanotube solution (in distilled water) was dispensed onto the patterned PDMS substrate after an oxygen plasma treatment with the 5 mbar, 50 W for 1 min to improve the adhesion between the PDMS and CNTs. After fast evaporating on the hotplate, the adhesive tape was removed to obtain a 2 × 2 pressure sensor array. Next, a 2 × 2 flexible TS-based array backplane was fabricated by following the same process of the preparation of individual TS device, except the shadow masks with an interconnection Au layer. Finally, the CNT pressure sensor array was directly laminated on the flexible TS-based array backplane to form a fully

integrated pressure sensor array.

Electrical and Mechanical Measurements: The current–voltage (I–V) characteristics and constant voltage stress were performed using a Keithley 4200 semiconductor device parameter analyzer. Arbitrary waveform generators (Agilent 33220A) and an oscilloscope (Tektronix DPO5054B) were used to generate pulse wave and monitor the fast current response flowing through the flexible TS device. During the pulse measurement, a 1 MΩ resistor was connected in series to the flexible TS device to serve as a current limiter. The cycle testing of mechanical bending was carried out by MTS Criterion Model 42. The TS behavior of the flexible TS device was measured after it recovered to the flat state

Reference

1. Webb, R.C. et al. Ultrathin conformal devices for precise and continuous thermal characterization of human skin. *Nat. Mater.* **12**, 938-944 (2013).
2. Lipomi, D.J. et al. Skin-like pressure and strain sensors based on transparent elastic films of carbon nanotubes. *Nat. Nanotechnol.* **6**, 788-792 (2011).
3. Ji, Y. et al. Flexible and twistable non-volatile memory cell array with all-organic one diode-one resistor architecture. *Nat. Commun.* **4**, 2707 (2013).
4. Son, D. et al. Multifunctional wearable devices for diagnosis and therapy of movement disorders. *Nat. Nanotechnol.* **9**, 397-404 (2014).
5. Sekitani, T. et al. Organic nonvolatile memory transistors for flexible sensor arrays. *Science* **326**, 1516-1519 (2009).
6. Gao, W. et al. Fully integrated wearable sensor arrays for multiplexed in situ perspiration analysis. *Nature* **529**, 509-514 (2016).
7. Someya, T. et al. A large-area, flexible pressure sensor matrix with organic field-effect transistors for artificial skin applications. *Proc. Natl Acad. Sci.* **101**, 9966-9970 (2004).
8. Someya, T. et al. Conformable, flexible, large-area networks of pressure and thermal sensors with organic transistor active matrixes. *Proc. Natl Acad. Sci.* **102**, 12321-12325 (2005).
9. Sobel, A. Electronic paper: high-speed inks. *Nat. Mater.* **2**, 643 (2003).
10. Takei, K. et al. Nanowire active-matrix circuitry for low-voltage macroscale artificial skin. *Nat. Mater.* **9**, 821-826 (2010).
11. Gelinck, G.H. et al. Flexible active-matrix displays and shift registers based on solution-processed organic transistors. *Nat. Mater.* **3**, 106-110 (2004).
12. Shulaker, M.M. et al. Three-dimensional integration of nanotechnologies for computing and data storage on a single chip. *Nature* **547**, 74-78 (2017).
13. Yang, J.J., Strukov, D.B. & Stewart, D.R. Memristive devices for computing. *Nat. Nanotechnol.* **8**, 13-24 (2013).

14. Midya, R. et al. Anatomy of Ag/Hafnia-based selectors with 10^{10} nonlinearity. *Adv. Mater.* **29** (2017).
15. Wang, Z. et al. Memristors with diffusive dynamics as synaptic emulators for neuromorphic computing. *Nat. Mater.* **16**, 101-108 (2017).
16. Han, U.-B., Lee, D. & Lee, J.-S. Reliable current changes with selectivity ratio above 10^9 observed in lightly doped zinc oxide films. *NPG Asia Mater.* **9**, e351 (2017).
17. Choi, B.J. et al. Trilayer Tunnel Selectors for Memristor Memory Cells. *Adv. Mater.* **28**, 356-362 (2016).
18. Lee, W. et al. High current density and nonlinearity combination of selection device based on $TaO_x/TiO_2/TaO_x$ structure for one selector–one resistor arrays. *ACS Nano* **6**, 8166–8172 (2012).
19. Wang, M. et al. Conduction mechanism of a TaO_x-based selector and its application in crossbar memory arrays. *Nanoscale* **7**, 4964-4970 (2015).
20. Hsiung, C.-P. et al. Formation and instability of silver nanofilament in Ag-based programmable metallization cells. *ACS Nano* **4**, 5414-5420 (2010).
21. Valov, I. et al. Nanobatteries in redox-based resistive switches require extension of memristor theory. *Nat. Commun.* **4**, 1771 (2013).
22. Hurk, J.V.D., Linn, E., Zhang, H., Waser, R. & Valov, I. Volatile resistance states in electrochemical metallization cells enabling non-destructive readout of complementary resistive switches. *Nanotechnology* **25**, 425202 (2014).
23. Ambrogio, S., Balatti, S., Choi, S. & Ielmini, D. Impact of the mechanical stress on switching characteristics of electrochemical resistive memory. *Adv. Mater.* **26**, 3885-3892 (2014).
24. Chae, B.G. et al. Nanometer-scale phase transformation determines threshold and memory switching mechanism. *Adv. Mater.* **29** (2017).
25. Wang, H. et al. Configurable resistive switching between memory and threshold characteristics for protein-based devices. *Adv. Funct. Mater.* **25**, 3825-3831 (2015).
26. Sun, H. et al. Direct observation of conversion between threshold switching and memory switching induced by conductive filament morphology. *Adv. Funct. Mater.* **24**, 5679-5686 (2014).
27. Xu, F. & Zhu, Y. Highly conductive and stretchable silver nanowire conductors. *Adv. Mater.* **24**, 5117-5122 (2012).
28. Chang, S.H. et al. Occurrence of both unipolar memory and threshold resistance switching in a NiO film. *Phys. Rev. Lett.* **102**, 026801 (2009).
29. He, L. et al. Memory and threshold resistance switching in Ni/NiO core-shell nanowires. *Nano Lett.* **11**, 4601-4606 (2011).
30. Son, M. et al. Excellent selector characteristics of nanoscale VO_2 for high-density bipolar ReRAM applications. *IEEE Electron Device Lett.* **32**, 1579 (2011).
31. Mannsfeld, S.C. et al. Highly sensitive flexible pressure sensors with microstructured rubber dielectric layers. *Nat. Mater.* **9**, 859-864 (2010).
32. Liu, Y. et al. Stretchable motion memory devices based on mechanical hybrid materials. *Adv. Mater.* **29** (2017).
33. White, S.I., Vora, P.M., Kikkawa, J.M. & Winey, K.I. Resistive switching in bulk silver nanowire-polystyrene composites. *Adv. Funct. Mater.* **21**, 233-240 (2011).
34. Gurski, K.F., McFadden, G.B. & Miksis, M.J. The effect of contact lines on the rayleigh instability with anisotropic surface energy. *SIAM J. Appl. Math.* **66**, 1163-1187 (2006).

35. Shi, Y. et al. In situ demonstration of the link between mechanical strength and resistive switching in resistive random-access memories. *Adv. Electron Mater.* **1**, 1400058 (2015).
36. Zhu, B. et al. Microstructured graphene arrays for highly sensitive flexible tactile sensors. *Small* **10**, 3625-3631 (2014).
37. Kim, S. et al. Flexible crossbar-structured resistive memory arrays on plastic substrates via inorganic-based laser lift-off. *Adv. Mater.* **26**, 7480-7487 (2014).
38. Linn, E., Rosezin, R., Kugeler, C. & Waser, R. Complementary resistive switches for passive nanocrossbar memories. *Nat. Mater.* **9**, 403-406 (2010).

Acknowledgements

The authors thank Dr. Naoji Matsuhisa for valuable discussions. They also thank the financial support from the National Research Foundation (NRF), Prime Minister's office, Singapore, under its NRF Investigatorship (NRF2016NRF-NRF1001-21), Singapore Ministry of Education (MOE2014-T2-2-140 and MOE2015-T2-2-60), K. C. Wong Education Foundation. Also thank the financial support from European Research Council (ERC) under the European Union's Horizon 2020 research and innovation programme (grant agreement No. 648635).

Supporting Information

Supporting Information is available from the Wiley Online Library or from the author.

Competing financial interests

The authors declare no competing financial interests.

Keywords

flexible sensory arrays, flexible threshold switches, highly nonlinear, matrix addressing, nanocontacts

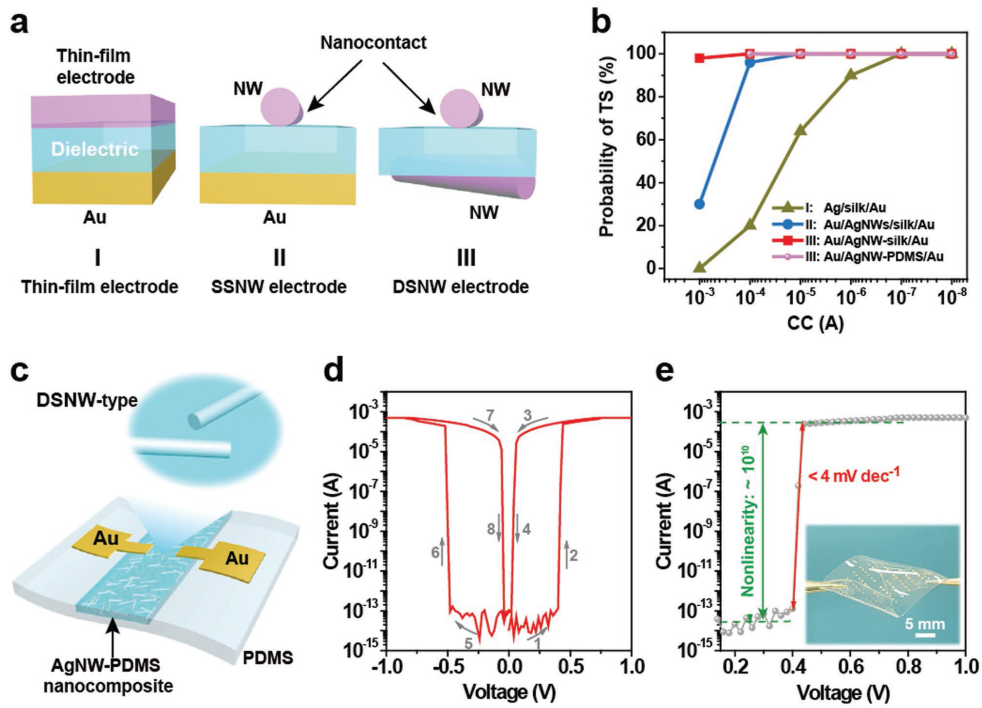

Figure 1 | Nano-contact induced highly-nonlinear flexible TS device. a, Schematic showing the configuration of TS devices with different contact morphology. I: device with a thin-film electrode, II: device with a single-side nanowire (SSNW) electrode configuration, III: device with a double-side nanowire (DSNW) electrode configuration. **b,** Probability of TS as a function of the CC for devices I, II, III. For simplicity of the device preparation, device I: Ag/silk/Au, device II: Ag/AgNWs/silk/Au, and device III: Ag/AgNWs-silk/Au are used to illustrate the nano-contact strategy. The probability of TS under high CC was significantly improved in the nano-contact type devices (II and III), regardless of dielectrics (silk or PDMS). **c,** Schematic of the flexible TS device with two-terminal Au/AgNWs-PDMS/Au planar structure. By utilizing the natural nano-contacts of AgNWs in the nanocomposite thin film, we achieved a DSNW-type flexible TS device (inset). **d,** Typical *I–V* characteristics of the flexible TS device with super nonlinear, bidirectional, and low voltage TS behavior. **e,** Flexible TS device with a super nonlinearity of ~ 10^{10} at V_D = 0.5 V and a fast turn-on switching slope of < 4 mV • dec^{-1}. Inset of **(e)** shows the optical-microscope image of the fabricated flexible TS device under bending state.

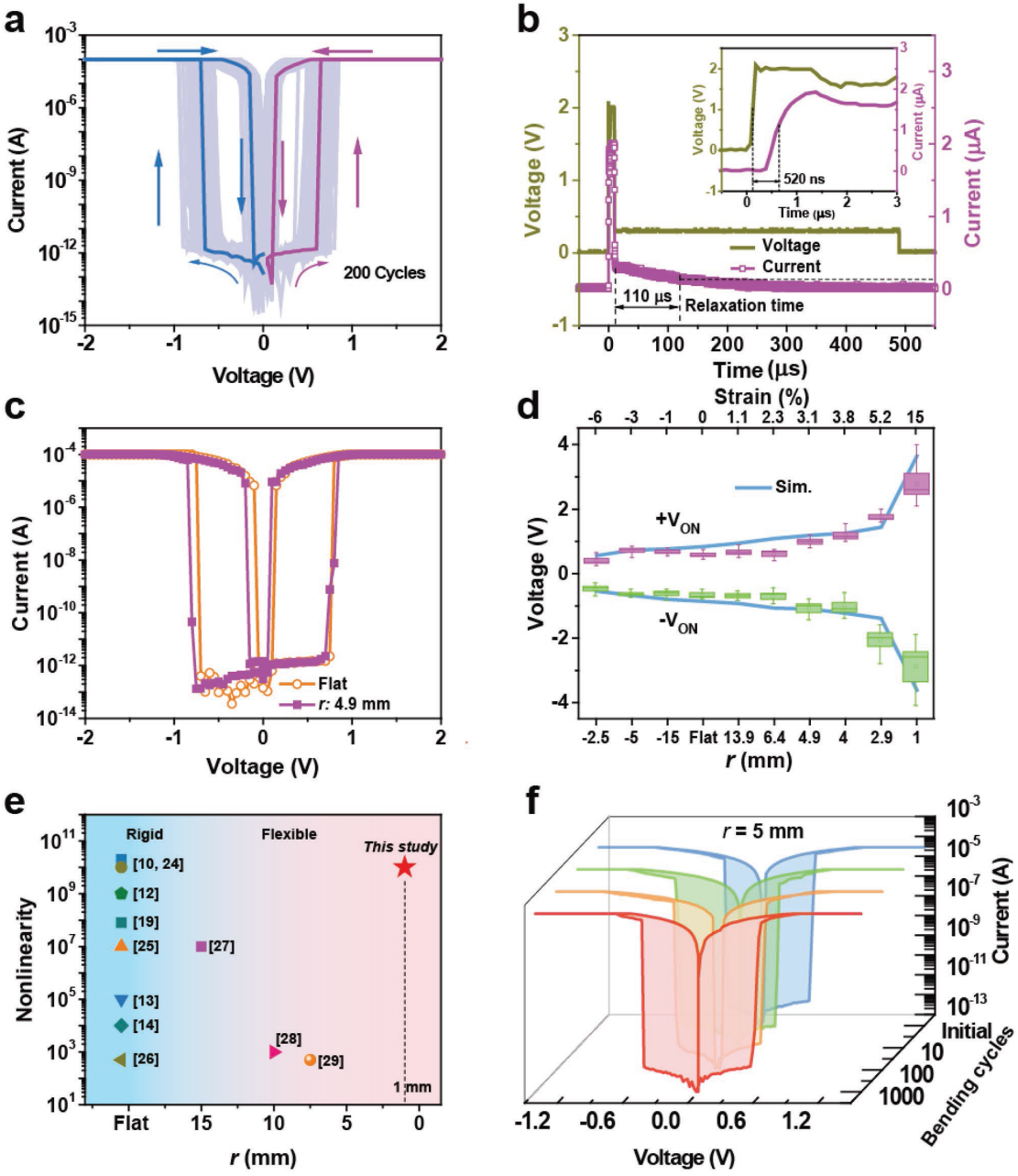

Figure 2 | Electrical characteristics and mechanical stability of flexible TS device. a, Consecutive 200 cycles of DC voltage sweeps with CC of 100 μA show no deterioration. Positive and negative voltage sweeps were alternately applied. **b,** Dynamical response characteristics of the flexible TS device. The device can be turned on fast (520 ns; see inset) under a 10 μs / 2 V pulse, and then turned off spontaneously after removing the external electric field. The relaxation time (defined as the time required for the conductance to drop to 1/e of the maximum conductance value after the removal of the turn-on voltage) is around 110 μs as verified by a following pulse of 480 μs / 0.3 V. **c,** Endurance of the flexible TS device with 10^6 cycles under the 100

μs/2 V programming pulses and 100 μs/0.3 V read pulses, with a 1.8 ms wait time between each program and read pulse. In **(b)** and **(c)**, a fixed resistor (1 MΩ) was connected in series to the flexible TS device to sever as a current limiter. **d,** *I-V* characteristics of the flexible TS device under both flat and bent state with a bending radius of 4.9 mm. No obvious change seen under the bent state. **e,** Distribution of $+V_{ON}$ and $-V_{ON}$ under both inward bending ($r < 0$) and outward bending ($r > 0$) as a function of r^{-1} from – 0.4 mm^{-1} to 1 mm^{-1}. Each error bar chart was collected from 5 cycles. Good consistency between the experimental and simulated ('sim' blue line) results based on molecular dynamics model. **f,** *I-V* characteristics of the flexible TS device under consecutive 1000 mechanical bending cycles show no noticeable deterioration. The bending radius *r* is 5 mm.

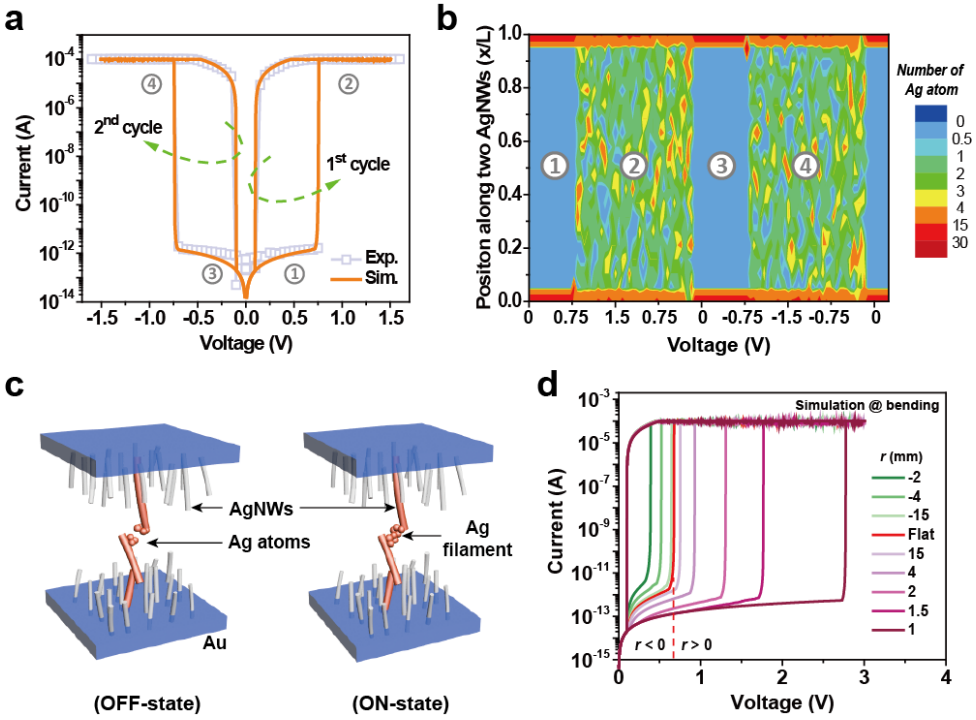

Figure 3 | Simulation of molecular dynamics model. a, Simulated and experimental *I-V* characteristics of the flexible TS device show good agreement, validating the molecular dynamics Langevin model. CC: 0.1 mA. **b,** Simulated dynamic evolution of the nanoscale Ag filament between the critical adjacent AgNWs over two sweep cycles. 1st sweep cycle: applied voltage (0 V → 1.5 V → 0 V); 2nd sweep cycle: applied voltage (0 V → -1.5 V → 0 V). ○,1, ○,2, ○,3, ○,4 represent the node times when the applied voltages are 0.5 V, 1.2 V, -0.5 V, -1.2 V, respectively. With the applied voltage sweeping, Ag nanoparticles could form a conductive filament under high electrical field, and recover to their original positions as the electrical field decreases. Color bar represents the numbers of Ag atoms. In the initial state (0 V), there are totally 60 Ag atoms equally distributed within the two critical adjacent AgNWs. **c,** Schematic illustration of the flexible TS device switched between OFF-state and ON-state. Red cylinders represent the critical adjacent AgNWs. **d,** Simulated results at positive sweep voltage of the TS behaviors of flexible TS device under different bending radius are consistent with our experimental results shown in Fig. 2**e**. '-': inward bending ($r < 0$), '+': outward bending ($r > 0$). Similar simulated result for the negative TS behaviors is in Supplementary Fig. 12d.

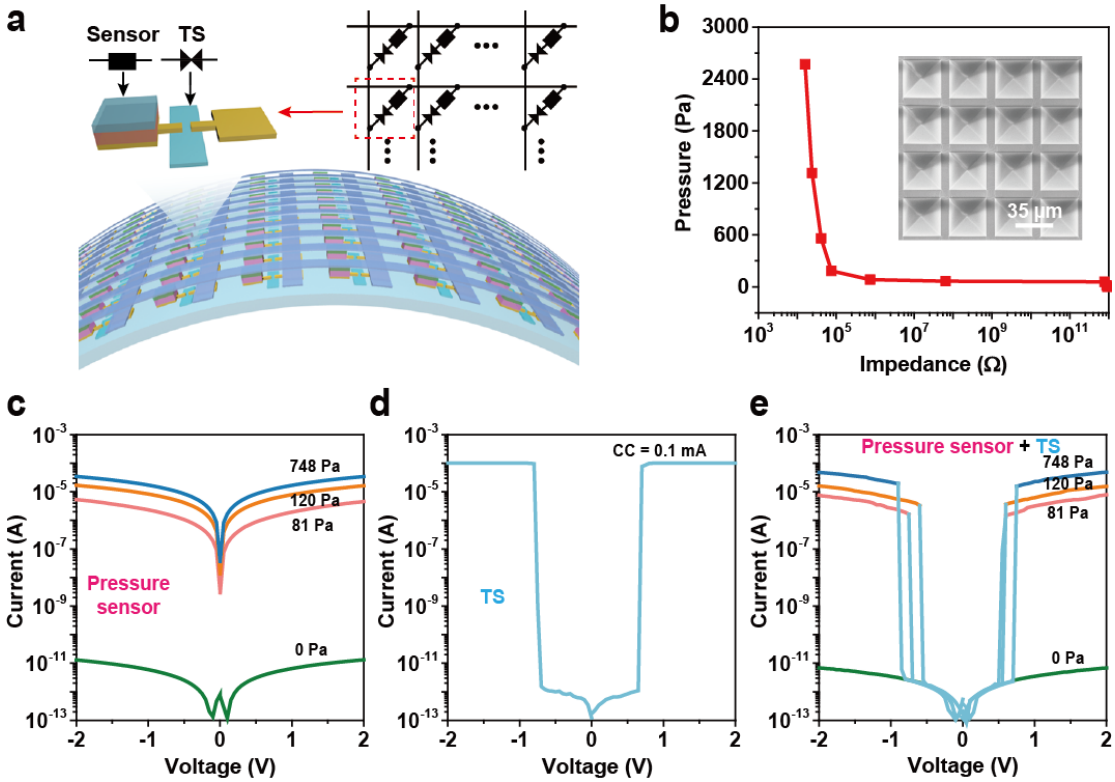

Figure 4 | Operating principle of the flexible TS-based sensory array. a, Schematic showing the configuration of the integrated crossbar array of sensors based on the two-terminal flexible TS devices. Left inset: Each integrated unit in the cross-point consists of a flexible TS device and a functional sensor element connected in series. Right inset: schematic of the corresponding circuit. **b,** Ultrasensitive pressure-impedance sensing characteristics of the CNT pressure sensor. Inset shows the SEM image of pressure sensor with pyramidal microstructures. **c,** Linear *I-V* relationship of individual pyramidal pressure sensor within an integrated unit under four different load pressures (0 Pa, 81 Pa, 120 Pa, 748 Pa). **d,** Threshold *I-V* relationship of individual flexible TS device in the same integrated unit. **e,** Threshold sensing characteristics of the integrated unit under different load pressures. Current levels at low bias voltage (< 0.6 V) are suppressed by the flexible TS device. By setting V_D = 0.8 V, the nonlinearity of integrated unit reaches up to 10^8 for load pressure of 748 Pa.

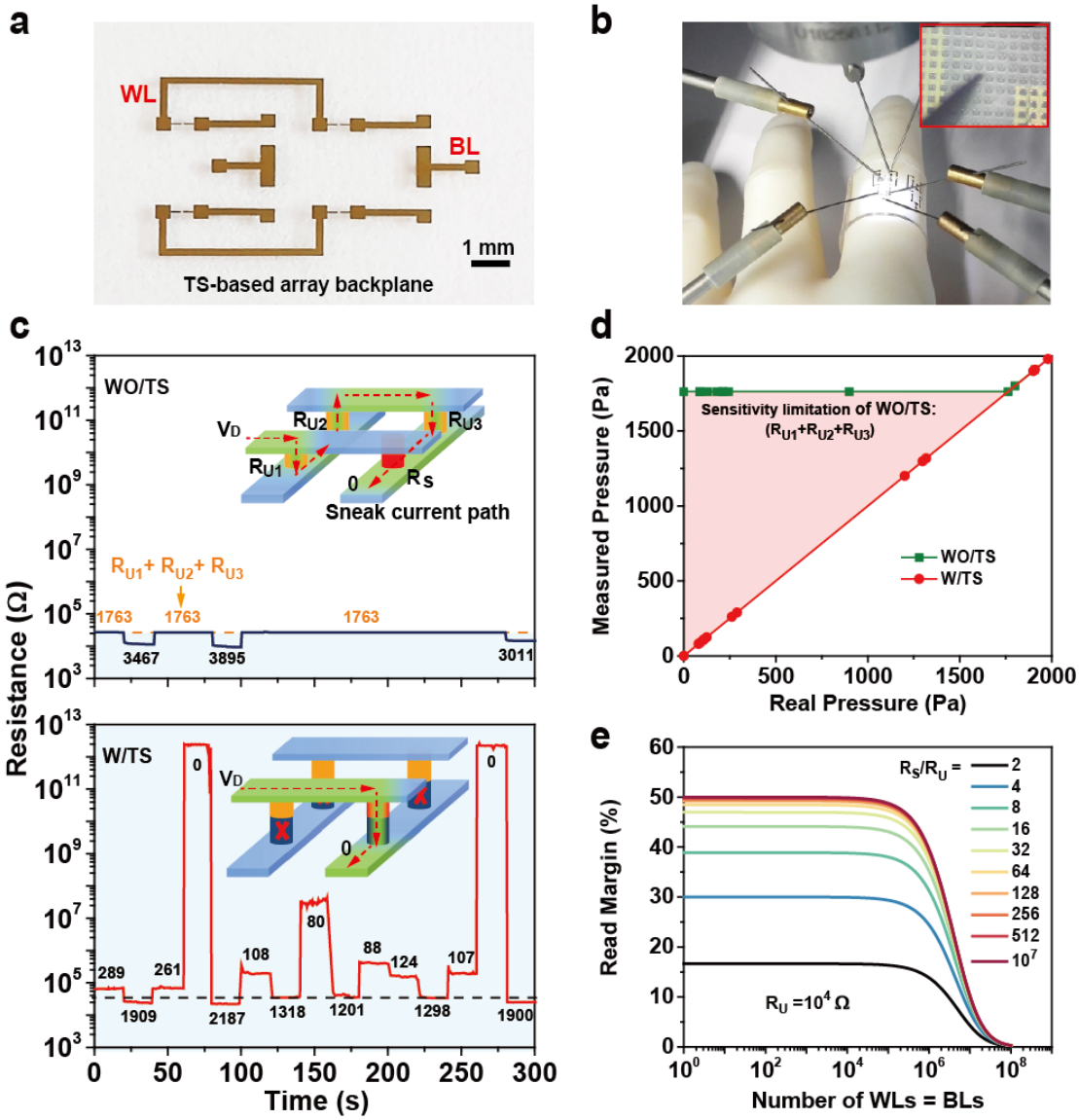

Figure 5 | Improving the readout range of fully integrated flexible TS-based sensory array. a, Optical image of the fabricated 2 × 2 flexible TS-based array backplane. **b,** Measurement setup of the flexible TS-based pressure sensor array. The CNT pressure sensor array was fixed on a hand replica and a probe station system was used to provide the real load pressure. Inset shows the enlarge image of a CNT pressure sensor under a load pressure state. **c,** Continuous sensing resistance of a selected pixel under different pressure levels in both WO/TS and W/TS array. Insets illustrate the corresponding current path in a worst-case scenario, where the undesired sneak current path is eliminated effectively. **d.** Enabled readout range of a selected pixel in both WO/TS and W/TS array. The enabled readout range of WO/TS array considerably degrades due to the sneak current flowing through three unselected sensors (R_{U1} + R_{U2}

+ R_{U3}), as shown in the upper inset in **(c)**. **e,** Normalized read margin versus number of WLs (WLs = BLs) for a flexible integrated pressure sensor array at the worst-case scenario. Herein, we assumed $R_U = 10^4$ Ω for all unselected pixels, and R_S/R_U = 2, 4, 8, 16, 32, 64, 128, 256, 512 and 10^7 for selected pixels. The calculated maximum array size can reach up to 10^7.

Supplementary Information for

Highly-nonlinear flexible threshold switch for the selection of sensory arrays

Ming Wang[1], Wei Wang[2], Wan Ru Leow[1], Changjin Wan[1], Geng Chen[1], Yi Zeng[1], Jiancan Yu[1], Yaqing Liu[1], Pingqiang Cai[1], Daniele Ielmini[2†] and Xiaodong Chen[1†]

Table of Contents:

I: Supplementary Text

II: Supplementary Figure and Caption

III: Supplementary References:

[†]Corresponding author. E-mail: daniele.ielmini@polimi.it; chenxd@ntu.edu.sg

I: Supplementary Text

1. Fabrication process of control devices I, II, and III

Silver nanowires (AgNWs) with a diameter of 60 nm and a length of 10 μm were purchased from Sigma-Aldrich. The aqueous solution of silk fibroin for fabricating these three devices I, II, and III was prepared according to the method described in our previous reports[1]. Firstly, *Bombyx mori* cocoons were boiled for 1 h in 0.02 M Na_2CO_3 and rinsed thoroughly with distilled water in order to remove the sericin protein on the surface of fibroin fibers. The dry fibroin fibers were then dissolved in 9.3 M LiBr solution at 60 °C for 4 h. Subsequently, the dissolved solution was dialyzed in distilled water in order to remove the traces of LiBr for six times. The solution after dialyzed was then centrifuged at the speed of 10000 rpm for 5 min to achieve the resultant aqueous solution.

For all control devices, Cr/Au films with the thickness of 5 nm/70 nm were subsequently deposited by thermal evaporator on a SiO_2/Si substrate as the bottom electrodes.

Device I: 1% wt fibroin solution was spin coated onto the Au bottom electrode at 1000 rpm for 45 s, and then evaporated for 2 h in room temperature in the fume cupboard. A 70 nm-thickness Ag pad with the size of 100 μm × 100 μm was deposited on silk fibroin film by thermal evaporator as active thin film electrode (Supplementary Fig. 1a).

Device II: The fabrication process of silk fibroin film is the same to that of device I. Then, 0.01% wt AgNWs solution diluted by IPA was sprayed on the silk fibroin film by inkjet printing method. At last, a 70 nm-thickness Au layer was thermally evaporated onto the silk fibroin film covered by a very small amount of AgNWs. The pattern size of Au layer is also 100 μm × 100 μm. However, in this configuration, the effective contact area of top electrode is region covered by AgNWs, because only the AgNWs would provide the mobile ions to trigger threshold switching (TS). This contact between the AgNWs and silk fibroin film is in the nano-scale range due to the cylindrical structure of AgNWs. Hence, device II is a SSNW-type configuration with nano-contact

(Supplementary Fig. 1b).

Device III: In order to obtain DSNW-type device, 0.5% wt AgNWs solution (0.2 ml) was mixed with 2% wt silk fibroin solution (1 ml). The resultant blended solution was used to spin coat onto the Au bottom electrode at 1000 rpm for 45 s, and then evaporated for 2 h in room temperature in the fume cupboard. Then, a 70 nm-thickness Au layer pad with the size of 100 μm × 100 μm was deposited on silk fibroin film by thermal evaporator. Since the concentration of AgNWs in blended solution is very dilute, the as-prepared Au/AgNWs-Silk/Au device shows high initial OFF resistance state. For this device, the effective active electrodes are equivalent to two AgNWs. Hence, device III is a DSNW-type configuration (Supplementary Fig. 1c).

2. Calculation of read margin of the flexible TS-based pressure sensor array

Modelling for calculation of read margin:

To simplify the analyses of various read schemes, we make two assumptions as follows: (1) the conducting line resistance can be neglected, so that all voltage drops occur across the pull-up resistances and cross-bar junctions. (2) The sensing resistance of pressure sensor is linear with the read voltage. Based on such assumptions, the *I-V* curve of the integrated unit with a pressure sensor element and a flexible TS element was represented using a threshold and pressure-dependent resistance, as follows:

$$R_{Sensing}(V) = \begin{cases} R_{TS-OFF}, & V_{-ON} < V < V_{+ON} \\ R_{TS-ON}(Pressure), & V \le V_{-ON}, V \ge V_{+ON} \end{cases}$$

Here, $R_{Sensing}$ is the real sensing resistance value of pressure sensor element; $R_{TS\text{-}OFF}$ is the OFF-state of FLEXIBLE TS element; $R_{TS\text{-}ON}$ is a function of applied pressure on the pressure sensor. In fact, $R_{Sensing}$ of the integrated unit is independent of the applied voltage (V). To read the pixel value in the targeted pixel position, a pull-up voltage (V_{pu}) is applied to the selected bit-line while the selected word line was grounded. The unselected bit lines can be either floating (one bit-line pull-up scheme, OBPU) or pulled-up (all bit-line pull-up scheme, ABPU)[2, 3], as shown in Supplementary Figure 14a. According to possible sneak current paths, unselected cells can be classified with

RI/RII/RIII, so that the N × N flexible pressure sensor array can be expressed by three resistors networks connected in series. Supplementary Figure 14b presents the equivalent circuit in OBPU read scheme.

Calculation of read margin at worst case scenario in OBPU scheme

In worst case scenario, all unselected pixels (R_U) are subject to maximum load pressure (MLP). According to the OBPU read scheme, the selected word line (WL) is biased to V_D and the selected bit line (BL) is biased to 0 V, while all the unselected WLs and BLs are floating. The equivalent circuit of the N × N flexible pressure sensor array can be further reduced as shown by Supplementary Figure 15a. By employing the Kirchhoff's equations, the voltage V_{out} across the selected pixels (R_S) can be calculated out. The read margin ($RM=\Delta V_{out}/V_{pu}$, where $\Delta V_{out} = V_{out,\,Sensing} - V_{out,\,MLP}$) criterion for determining the maximum crossbar array size is set to at least 10 % of pull-up voltage (V_{pu}). Herein, we assumed $R_U = 10^4$ Ω for all unselected pixels, and $R_S/R_U = 10^3$ for selected pixel. The calculated results of read margin with the flexible TS device (W/TS) and without the flexible TS device (WO/TS) are shown in the Supplementary Figure 15b.

II: Supplementary Figure and Caption

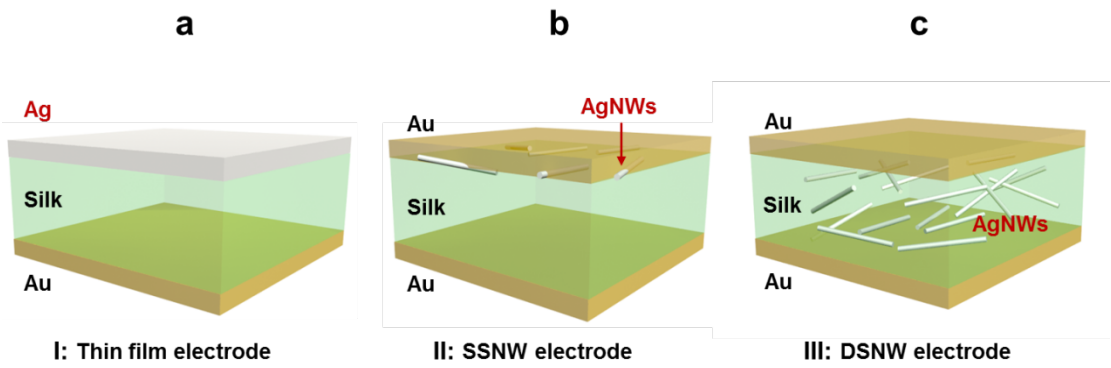

Supplementary Figure 1 Schematic illustration of devices I, II, and III. **(a)** I: thin film electrode configuration; **(b)** II: single-side nanowire (SSNW) configuration; **(c)** III: double-side nanowire (DSNW) configuration.

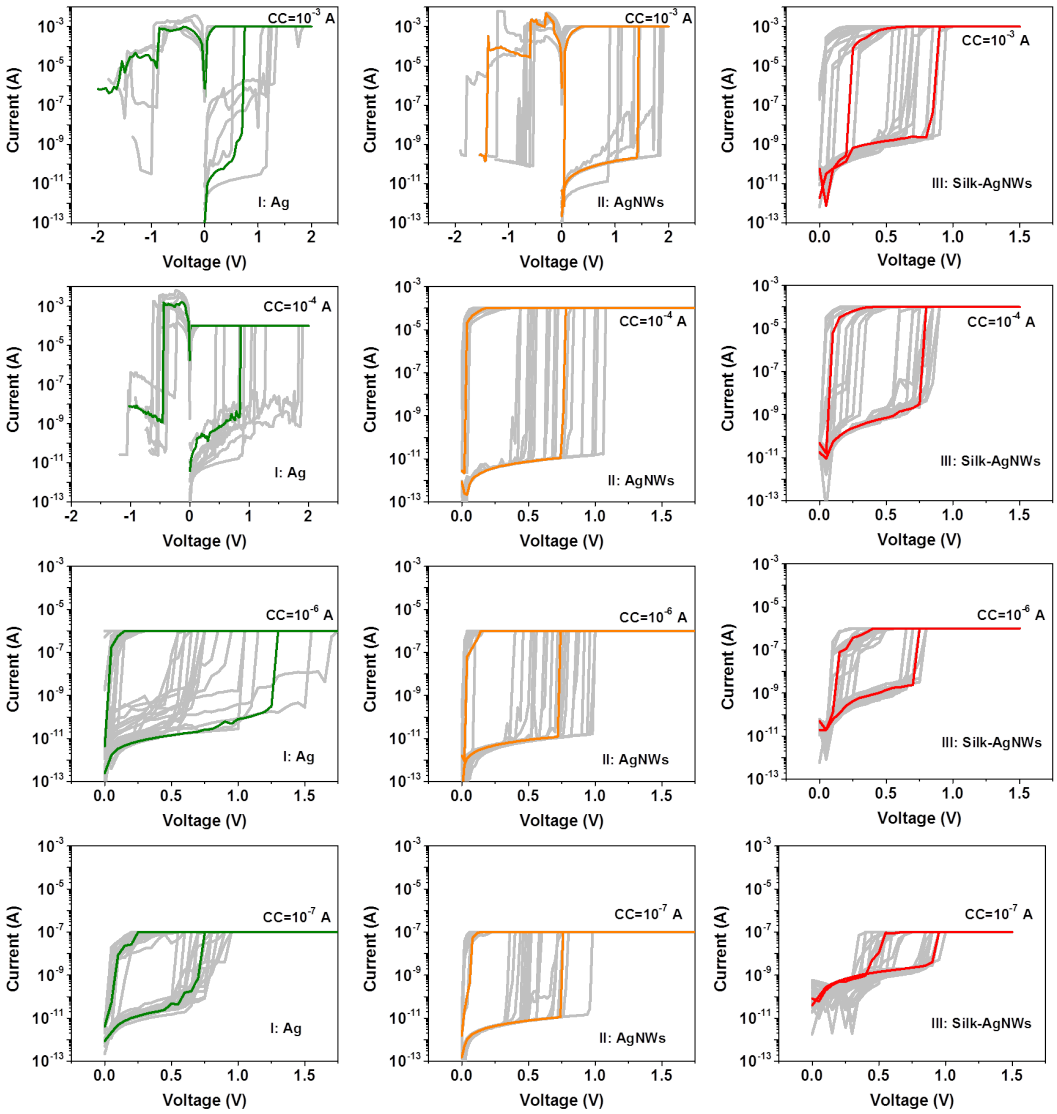

Supplementary Figure 2 Evolution of the current-voltage (*I-V*) characteristics as a function of CC for devices I, II, and III. Device I **(a, b, c, d)**, device II **(e, f, g, h)**, and device III **(i, j, k, l)**. Device I shows typical memory switching (MS) behavior for high CC (> 10^{-3} A) and TS behavior at low CC (< 10^{-7} A). Between 10^{-3} A and 10^{-7} A, both the MS and TS can be observed. Here, the criterion of TS behavior is defined as the retention time of ON-state resistance being less than 5 s. Both device II and device III significantly improve the maximum allowed CCs for reliable TS behavior due to the nano-contact effect. The maximum allowed CCs of reliable TS behavior for devices I, II, III are 10^{-7}, 10^{-4}, 10^{-3}A, respectively.

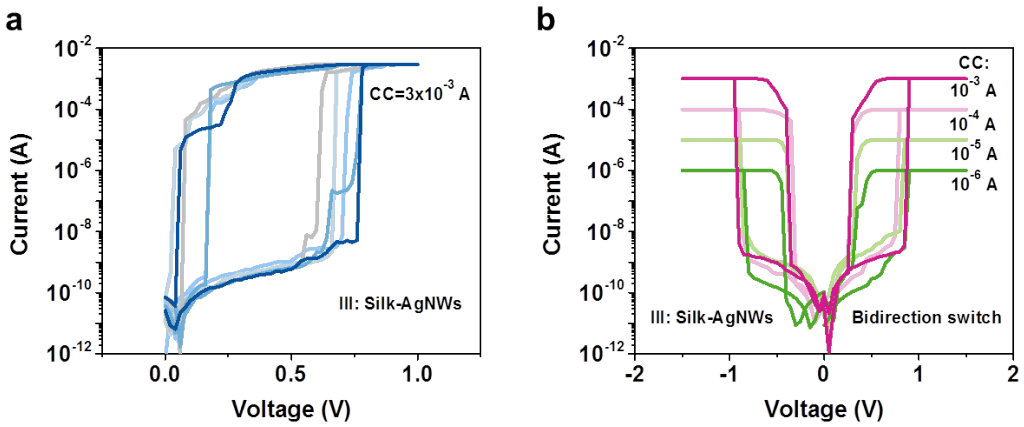

Supplementary Figure 3 Bidirectional and reliable TS behavior in device III. **(a)** Device III could still maintain TS behavior even for high CC of about 3 mA. **(b)** Bidirectional TS behavior at increasing CC levels.

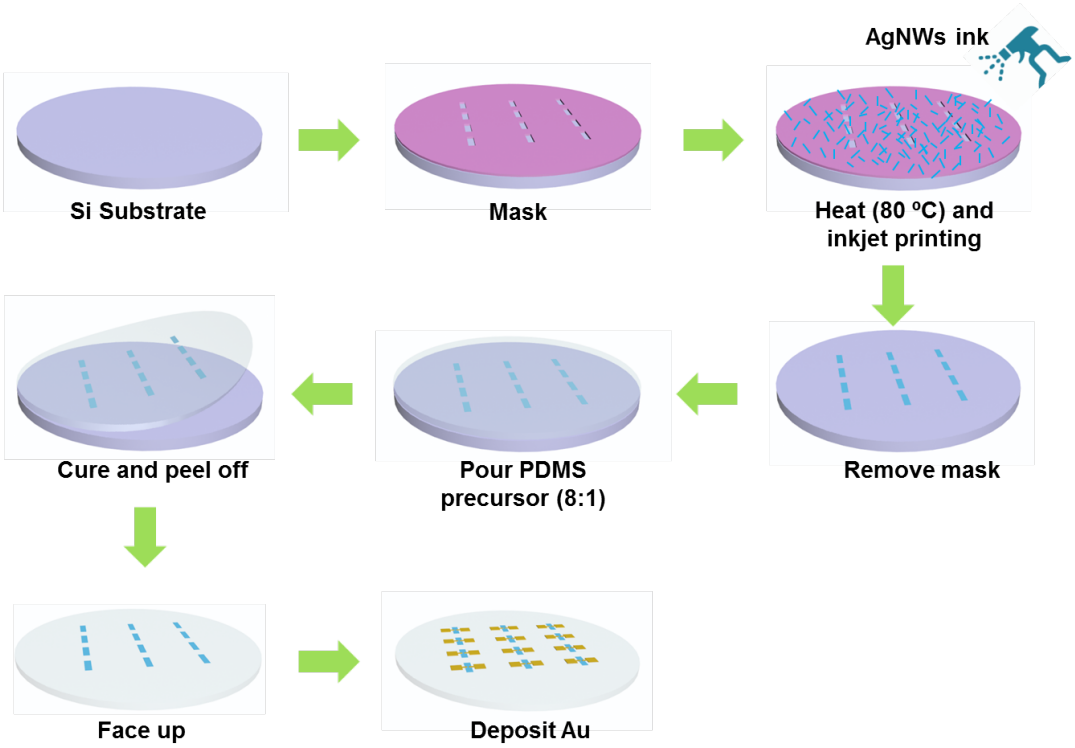

Supplementary Figure 4 Schematic illustration of the fabrication process for Au/AgNWs-PDMS/Au devices. Briefly, a patterned mask was firstly fixed on a silicon wafer after hydrophobization treatment. The diluted AgNWs solution was sprayed on the silicon substrate by inkjet printing method while keeping the substrate heating. Then, pour the PDMS precursor (8:1) and cure in 60℃ oven for 10 hours. At last, peel off and deposit gold (Au) electrode.

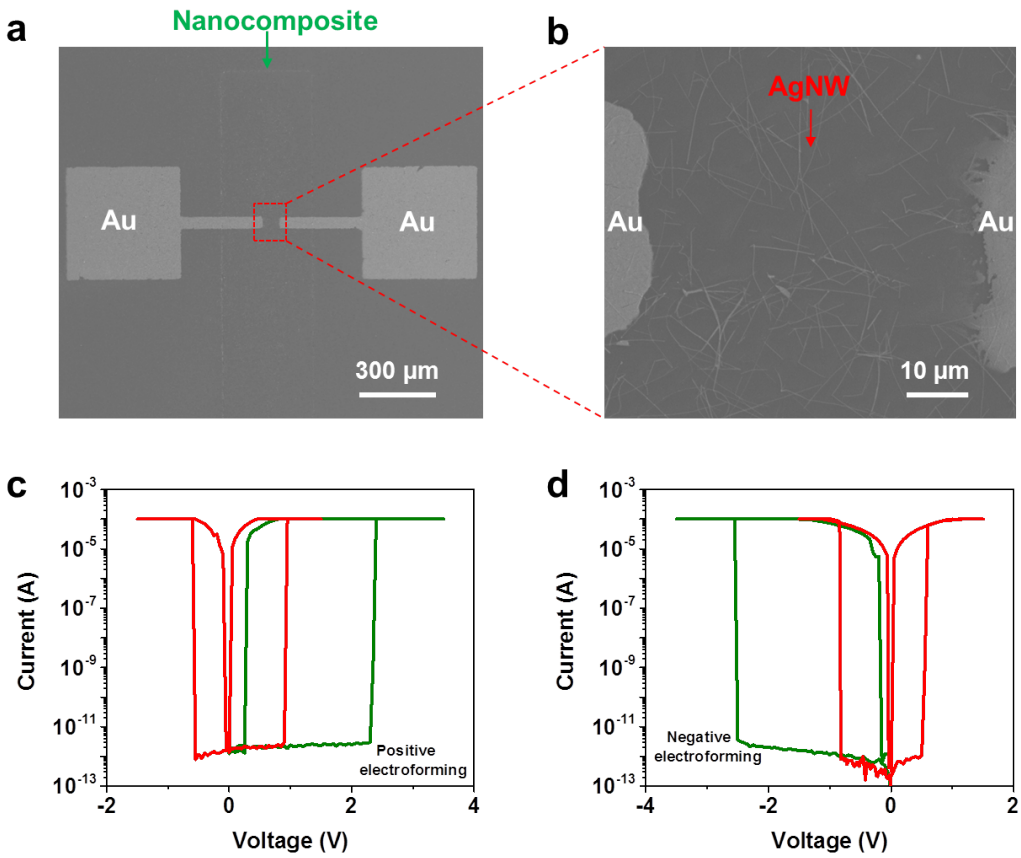

Supplementary Figure 5 Morphological and electrical characteristics of Au/AgNWs-PDMS/Au devices. **(a)** SEM image of the fabricated flexible TS device with two-terminal planar structure. **(b)** Enlarged SEM image of **(a)**. AgNWs were randomly embedded in the surface layer of PDMS matrices. Typical bidirectional TS behavior after positive electroforming process **(c)** and after negative electroforming process **(d)**, indicating no obvious dependence on the polarity of the initial forming process.

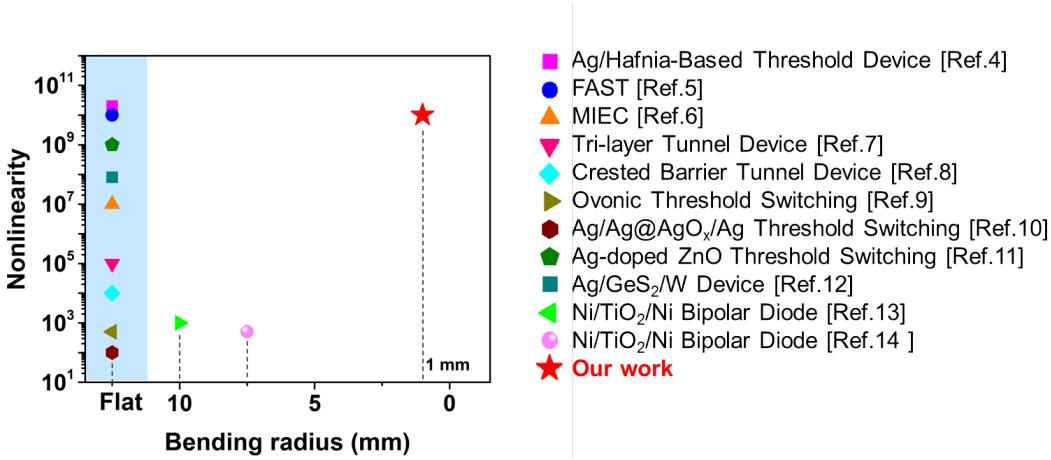

Supplementary Figure 6 Roadmap of various nonlinear electronic switches with two terminal and bidirectional characteristics. The Y-axis represents the nonlinearity; the X-axis represents the mechanical flexibility. Our demonstrated flexible TS device shows the highest nonlinearity reported in any type of flexible electronic switches[4-14].

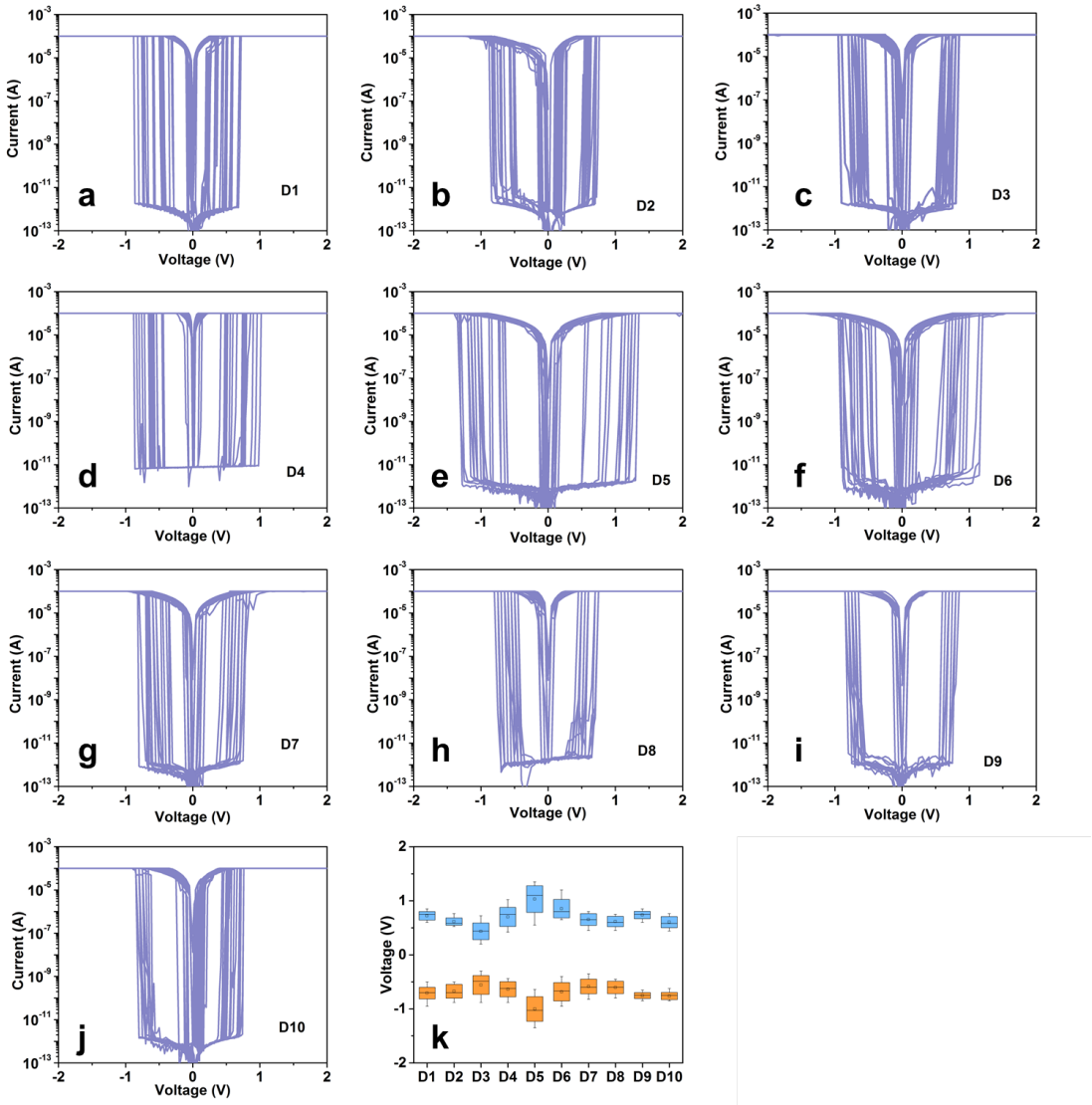

Supplementary Figure 7 The raw *I-V* characteristics of 10 selected flexible TS devices and the device-to-device uniformity of turn-on voltages.

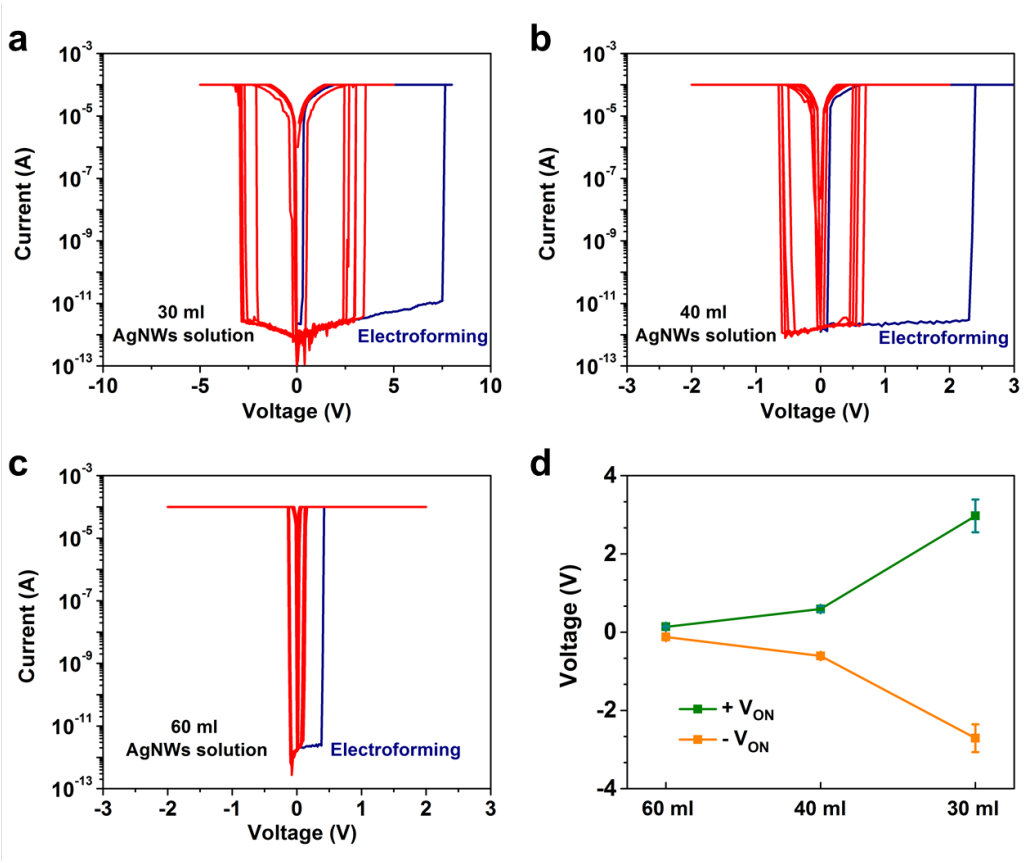

Supplementary Figure 8 Typical *I-V* curves of the flexible TS devices of different usage amounts (30 ml **(a)**, 40 ml **(b)** and 60 ml **(c)**) of AgNWs solutions for inkjet printing. The different usage amounts mean the different concentrations of AgNWs in nanocomposite. **(d)** Distribution of $+V_{ON}$ and $-V_{ON}$ with different concentrations of AgNWs.

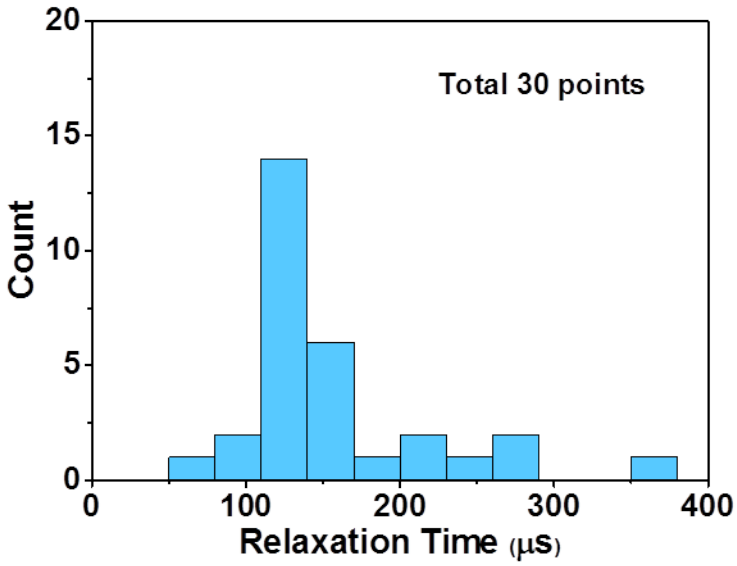

Supplementary Figure 9 Distribution of the relaxation time of the flexible TS device ranging from 50 μs to 400 μs.

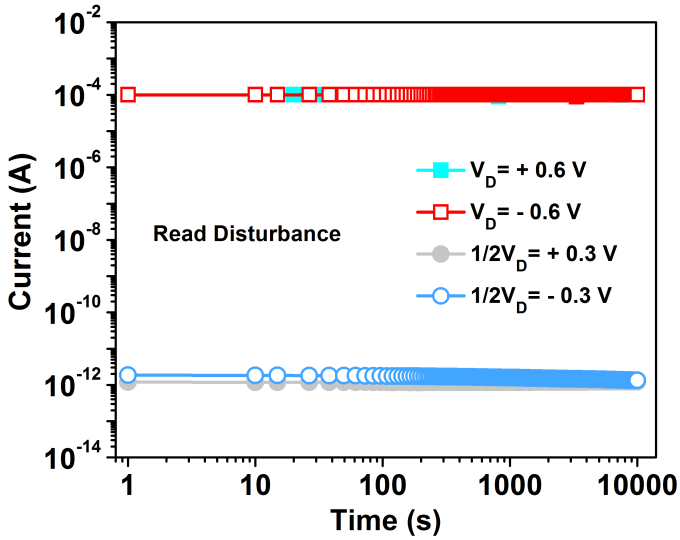

Supplementary Figure 10 Read disturbance of ON-state and OFF-state under constant voltage stress of $V_D = \pm 0.6$ V and $1/2V_D = \pm 0.3$ V.

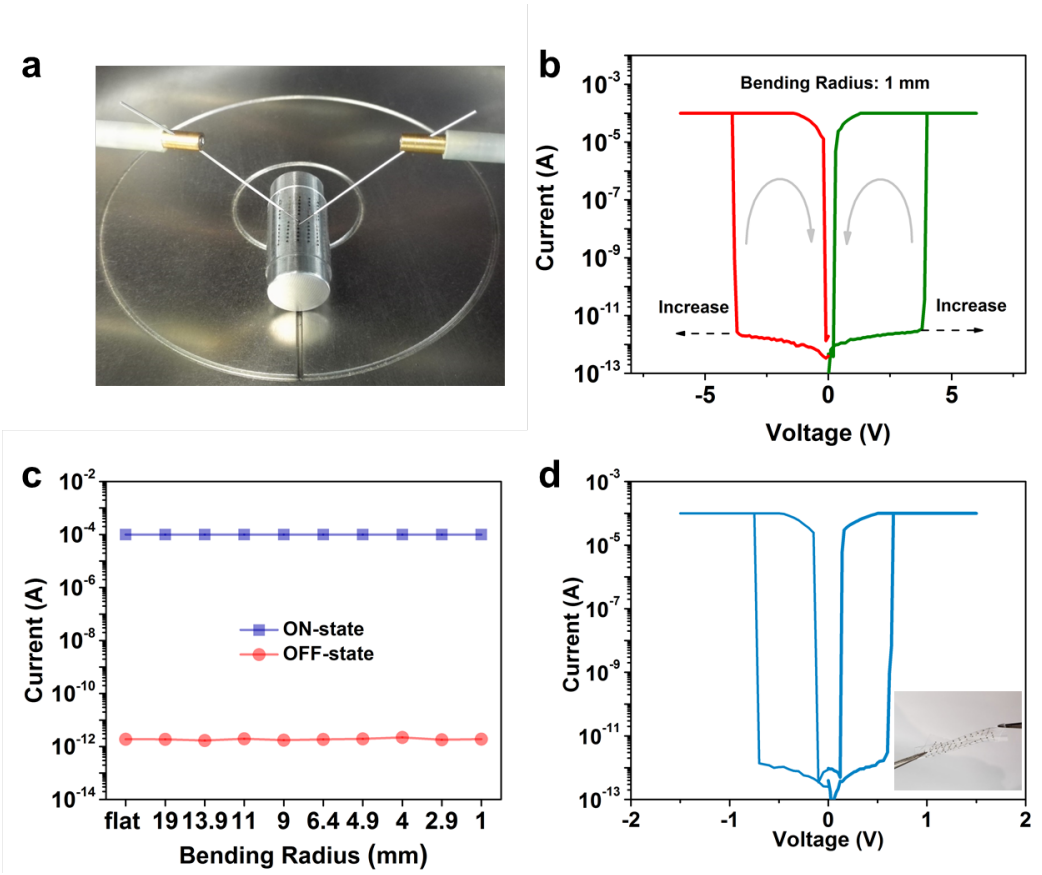

Supplementary Figure 11 Measurement setup and mechanical stability of the flexible TS device. **(a)** Experimental setup of mechanical stability by fixing the flexible TS device on the smooth cylinders with various diameters. **(b)** Typical *I-V* curves of the flexible TS device under the curved state with a bending radius of 1 mm. **(c)** The ON/OFF ratio of TS behavior of the flexible TS device as a function of bending radius *r* from flat to 1 mm. There is no noticeable deterioration in nonlinearity under all bending states. **(d)** Typical *I-V* curves of the flexible TS device after twisting in the right inset of (d).

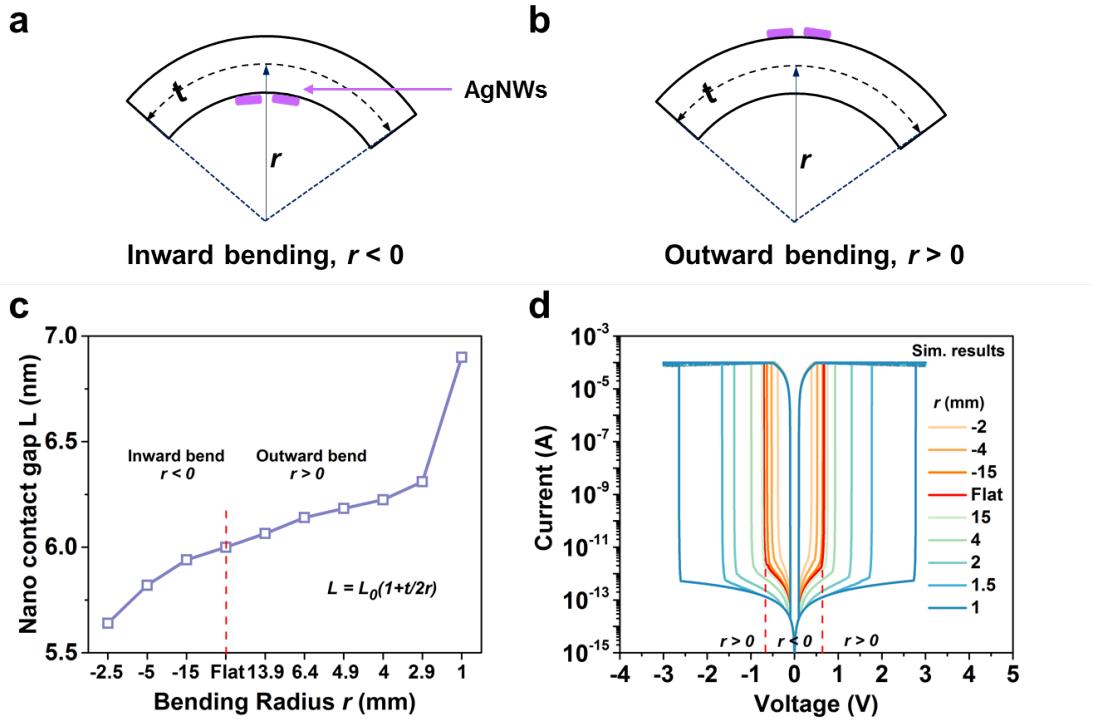

Supplementary Figure 12 (a) Inward bending state ($r < 0$). **(b)** Outward bending state ($r > 0$). **(c)** Calculated results of the nominal nano-contact gap under different bending radius. **(d)** Simulated *I-V* curves of the flexible TS device under different bending radius.

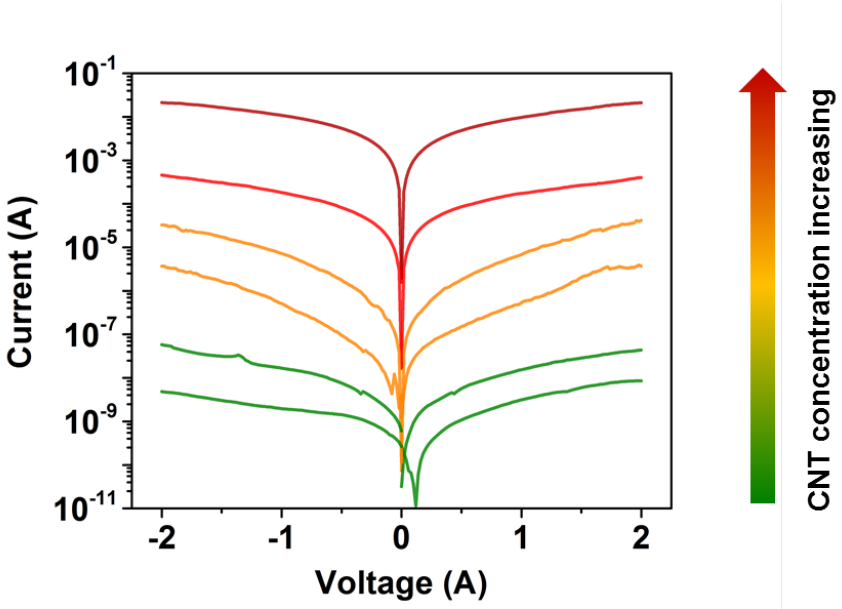

Supplementary Figure 13 *I-V* curves of the Au/CNTs-PDMS/Au controlled devices with various CNT concentrations. No reversible resistive switching behavior was observed in the *I-V* curves regardless of the concentration of CNTs.

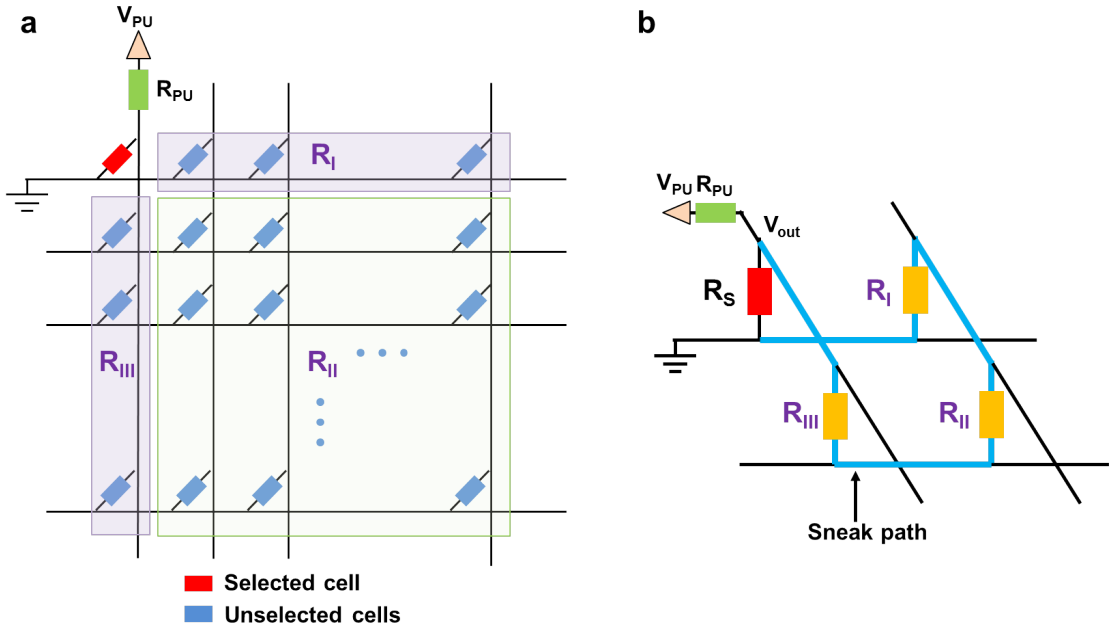

Supplementary Figure 14 (a) Crossbar array and periphery circuit of the One Bit-line Pull-Up scheme (OBPU) read scheme, (b) The equivalent circuit of OBPU read scheme.

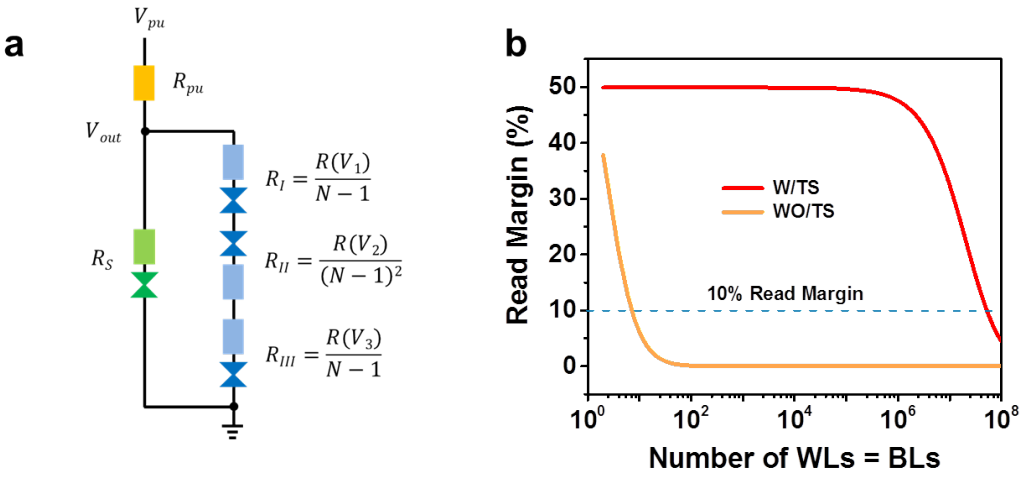

Supplementary Figure 15 (a) Equivalent circuit of N × N crossbar array using OBPU read scheme, (b) The calculated read margin with the flexible TS device (W/TS) and without the flexible TS device (WO/TS).

III: Supplementary References:

1. Wang, H. et al. Configurable resistive switching between memory and threshold characteristics for protein-based devices. *Advanced Functional Materials* **25**, 3825-3831 (2015).
2. Linn, E., Rosezin, R., Kugeler, C. & Waser, R. Complementary resistive switches for passive nanocrossbar memories. *Nature materials* **9**, 403-406 (2010).
3. Flocke, A. & Noll, T.G. in IEEE European Solid-State Circuits Conference (ESSCIRC) 328-331 (2007).
4. Midya, R. et al. Anatomy of Ag/Hafnia-based selectors with 10^{10} nonlinearity. *Advanced materials* **29** (2017).
5. Jo, S.H., Kumar, T., Narayanan, S., Lu, W.D. & Nazarian, H. in Electron Devices Meeting (IEDM) (IEEE International, 6.7.1-6.74; 2014).
6. Gopalakrishnan, K. et al. in Symposium on VLSI Technology Digest of Technical 205-206 (IEEE International, 2010).
7. Choi, B.J. et al. Trilayer tunnel selectors for memristor memory cells. *Advanced materials* **28**, 356-362 (2016).
8. Wootae Lee et al. High current density and nonlinearity combination of selection device based on TaO_x-TiO_2-TaO_x structure for one selector–one resistor arrays. *ACS Nano* **6**, 8166–8172 (2012).
9. Lee, M.J. et al. Two series oxide resistors applicable to high speed and high density nonvolatile memory. *Advanced materials* **19**, 3919-3923 (2007).
10. Du, H. et al. Engineering silver nanowire networks: from transparent electrodes to resistive switching devices. *ACS applied materials & interfaces* **9**, 20762-20770 (2017).
11. Han, U.-B., Lee, D. & Lee, J.-S. Reliable current changes with selectivity ratio above 10^9 observed in lightly doped zinc oxide films. *NPG Asia Materials* **9**, e351 (2017).
12. Ambrogio, S., Balatti, S., Choi, S. & Ielmini, D. Impact of the mechanical stress on switching characteristics of electrochemical resistive memory. *Advanced materials* **26**, 3885-3892 (2014).
13. Huang, J.-J., Tseng, Y.-M., Luo, W.-C., Hsu, C.-W. & Hou, T.-H. in Electron Devices Meeting (IEDM) 31.37.31-31.37.34 (IEEE International, 2011).
14. Kim, S. et al. Flexible crossbar-structured resistive memory arrays on plastic substrates via inorganic-based laser lift-off. *Advanced materials* **26**, 7480-7487 (2014).